

Article

Modelling Porous Cementitious Media with/without Integrated Latent Heat Storage: Application Scenario

Mona Nazari Sam ^{1,*} , Jens Schneider ²  and Holger V. Lutze ^{1,3,4}

¹ Department of Civil and Environmental Engineering, Institute IWAR, Chair of Environmental Analytics and Pollutants, Technical University of Darmstadt, 64297 Darmstadt, Germany; h.lutze@iwar.tu-darmstadt.de

² Institute of Structural Mechanics, and Design (ISM+D), Technical University of Darmstadt, 64297 Darmstadt, Germany; schneider@ismd.tu-darmstadt.de

³ IWW Water Centre, 45476 Mülheim an der Ruhr, Germany

⁴ Centre for Water and Environmental Research (ZWU), 45141 Essen, Germany

* Correspondence: nazarisammona@gmail.com

Abstract: This paper presents a methodological approach for the evaluation of the thermal behavior of cementitious porous media with/without integrated latent-heat thermal energy storage (LHTES). To achieve this goal, the Lewis-Nielsen model has been calibrated to predict the insulation properties of mineralized foamed concretes. Two pore-related microstructural fitting parameters, A and Φ_m , are presented according to the available data in the literature. In this regard, new findings are implemented for the classification of pore structure and prediction of the homogenized thermal conductivity of two-phase cementitious foams with or without phase change materials. The calibration and predictive analyses have been extended to a wide range of experimental data, including variation of binder types, porosities, and latent components. The presented analytical approach appears to agree well with experimental results and can be employed in the design of two-phase mineral foam materials. Then, to assess the thermal behavior of the predicted insulating envelopes, a one-dimensional (1D) enthalpy-based model is used which combines Fourier's law of heat conduction, the first law of thermodynamics, Lewis-Nielsen conductivities, and the mixture theory for LHTES additions. The results demonstrated the importance of volumetric heat capacity for the thermal inertia of building envelopes.

Keywords: latent heat thermal energy storage (LHTES); thermal energy storage (TES); porous media; cementitious foam; conductivity prediction; Lewis-Nielsen model; Fourier's law; dynamic envelopes; energy efficiency



Citation: Nazari Sam, M.; Schneider, J.; Lutze, H.V. Modelling Porous Cementitious Media with/without Integrated Latent Heat Storage: Application Scenario. *Energies* **2023**, *16*, 6687. <https://doi.org/10.3390/en16186687>

Academic Editors: Umberto Berardi and Davide Borelli

Received: 16 August 2023

Revised: 8 September 2023

Accepted: 13 September 2023

Published: 18 September 2023



Copyright: © 2023 by the authors. Licensee MDPI, Basel, Switzerland. This article is an open access article distributed under the terms and conditions of the Creative Commons Attribution (CC BY) license (<https://creativecommons.org/licenses/by/4.0/>).

1. Introduction

The built environment is responsible for over 30% of global energy consumption and contributes nearly 40% of total direct and indirect greenhouse gas emissions [1–3]. In this context, the use of thermal energy storage (TES) technologies and latent-heat thermal energy storage (LHTES) systems has an enormous potential for novel applications in buildings [4–6]. Utilizing phase-change materials (PCMs), one of the most effective methods for increasing the latent heat storage in buildings, offers viable solutions for improving energy efficiency, enhancing the performance of HVAC and on-site renewable energy systems, i.e., reducing peak loads, maintaining indoor comfort levels, regulating temperature excursions and attenuating extreme thermal values [7–11].

Over the past few years, numerous articles have been dedicated to exploring the use of PCMs in construction and building materials [12–14]. More specifically, the ability to store and release large amounts of heat into PCMs mixed within insulating envelopes can effectively reduce the thermal conditioning load of the building [15–24]. In this context, a significant proportion of the research on PCMs focuses on their incorporation into porous cementitious or other binder-based composites (i.e., having a density $<800 \text{ kg/m}^3$) to be

used for thermal insulation in nearly-zero-energy buildings (nZEB) [25–28]. These composites can provide excellent heat blocks and are non-flammable [29,30]. However, the thermophysical properties of cementitious foams largely depend on the microstructural parameters, including air content as well as inner pore morphology and the amount/type of binders, aggregates, and, eventually, additional components like fillers, fibers, or rubber particles [31–38]. The correlation between microstructural parameters and related thermophysical properties of porous cementitious composites has been the object of extensive study for many decades due to its wide applicability in engineering problems and applications.

From the modelling point of view, on one hand, several theoretical and empirical models have been proposed in the literature to deal with describing the conductivity (either thermal or electrical) of composites. In this context, the most popular expressions are those due to the proposals by Maxwell [39–42] and Bruggeman [43–46]. They are often based on expressions providing the effective conductivity of a homogenized composite, and built up by combining the conductivity of the multi-phase components, such as the matrix, fillers, air-voids, fibers, etc. The weighting parameters in these formulas are commonly determined by either the volumetric or the weight fraction of each individual phase. However, the influence of the pores (i.e., amounts, sizes, and distributions) on the heat-transfer properties of porous materials represents the key factor in this field [47]. Specifically, the thermal conductivity of two-phase porous systems has been reported to be strongly influenced by their pore nature and structure [48,49]. In this field, it is worth mentioning the proposal by Lewis and Nielsen [50,51], which most closely matches the transport parameters in two-phase porous systems in different cases [52–56].

On the other hand, modelling the heat storage capacity of porous cementitious systems enhanced with LHTES components has been largely explored in the literature. Most of the models arise from solving the so-called Stefan problem for phase transformation problems [57–59]. However, in construction and building materials applications, the problem can be highly simplified, and the so-called enthalpy-based method, employable for conduction-only mechanisms, represents the most used and simplified approach followed by many authors [60–65].

This study aims to propose a simplified analytical approach for predicting the homogenized thermal conductivity of porous cementitious media. A wide range of experimental data from the literature regarding the microstructure parameters of cement-based foams influencing thermal conductivity has been compiled. The links between air inclusions and fractions, geometrical classification of the pores, and the overall homogenized thermal conductivity k_{eff} of porous cementitious foams are established. The proposed analytical model concerns the stochastic characteristic of the pore structure and allows the prediction of the homogenized thermal conductivity of cementitious foams considering the shape and packing of the pores. The methodology can be further applied to solve the energy transport equations through the complex structure of mineral foams, with/without LHTES components, without the need for costly experimental designs or expensive computer analysis for ascertaining k_{eff} [66].

The present paper is structured as follows. Section 2 provides a summary of the available experimental data in the recent literature related to low-, medium-, and high-porosity cementitious media. In Section 3, the theoretical background of the Lewis-Nielsen model is discussed, including its assumptions, applicability, and further extension of the law. Section 4 presents the analytical predictions and comparisons relative to the experimental data to assess the soundness and capabilities of the methodology. Section 5 analyzes the TES (latent and sensible) performance of the studied composites, e.g., in 1D wall systems, while also examining the direct impacts of dynamic insulation parameters and the variable effusivity and diffusivity of the media. Finally, Section 6 concludes with the main remarks and provides future research directions.

2. Experimental Database

Experimental tests on variable porous cementitious systems have been employed as a reference database to show the potential and capability of the proposed modelling procedure described within Sections 3 and 4. This section reviews and analyzes a series of data available in the literature; the data cover the entire density (porosity) range, from low densities (porosities) up to high densities (porosities). The data are those tested by Batool (2015) [67], Awang et al. (2012) [68], Wei et al. (2013) [69], Mydin (2011) [70], Davraz et al. (2016) [71], Oren et al. (2020) [72], and Jiang et al. (2017) [73] & (2016) [74]; see Supplementary Material S1 for more details.

All data collected in Table 1 are highlighting the types of binders used, possible additives/fillers, target densities ρ , water-to-binder ratios, dry densities ρ , measured conductivity values of cementitious matrices/skeleton (either pastes or mortars), dispersed air content (porosity), type of foaming agent employed, methods of foaming, and measurement methods for the foam conductivity, as well as how all of these factors are affecting the overall conductivity of the foam system (last column of the table). The review of these data, as listed in Table 1, reveals that the use of different pozzolanic additives/fillers into the matrix can affect the porosity and the related properties of the foam, and generally leads to a reduction of the thermal conductivity of the composite.

Table 1. Experimental database of foam concrete by [67–74].

Authors	Binder Type	Additive/Filler	W/b Ratio	Target Density ρ (kg/m ³)	Dry Density ρ (kg/m ³)	Matrix Conductivity (k/W/m)	Dispersed Air Content ϵ	Foaming Agent	Foaming Method	Conductivity Measurement Method	Foam Conductivity (k/W/m)
Batool, F. (2015) [1]	HE portland cement	Ref	0.69	800	724	0.458	0.49	Synthetic	Physical air-entraining	Transient plane source (TPS)	0.180
				600	492	0.458	0.64				0.125
				400	303	0.458	0.78				0.076
		FA10		800	751	0.458	0.50				0.183
				600	549	0.458	0.62				0.136
				400	360	0.458	0.76				0.081
		FA20		800	710	0.407	0.50				0.182
				600	499	0.407	0.64				0.122
				400	273	0.407	0.81				0.074
		SF10		800	755	0.415	0.50				0.173
				600	499	0.415	0.65				0.111
				400	320	0.415	0.78				0.079
		SF20		800	750	0.416	0.53				0.166
				600	474	0.416	0.70				0.100
				400	270	0.416	0.83				0.071
		MK10		800	759	0.456	0.50				0.176
				600	529	0.456	0.65				0.119
				400	295	0.456	0.81				0.074
		MK20		800	756	0.461	0.51				0.179
				600	533	0.461	0.65				0.121
				400	276	0.461	0.82				0.074
Awang, H. et al. (2012) [2]	SEMI Portland cement/sand (1:1.5)	RefSa	0.45	600	n.a.	1.400	0.69	Protein-based	Physical air-entraining	Transient plane source (TPS)	0.190
				1000	n.a.	1.400	0.49				0.430
		FA15		1400	n.a.	1.400	0.36				0.590
				600	n.a.	n.a.	0.69				0.170
				600	n.a.	n.a.	0.70				0.160
		RL15		600	n.a.	n.a.	0.72				0.160
				600	n.a.	n.a.	0.70				0.200
				600	n.a.	n.a.	0.70				0.180
		PF40		600	n.a.	n.a.	0.71				0.180
				1000	n.a.	n.a.	0.50				0.380
				1000	n.a.	n.a.	0.51				0.360
		FA30		1000	n.a.	n.a.	0.56				0.310
				1000	n.a.	n.a.	0.55				0.310
				1000	n.a.	n.a.	0.54				0.310
		RL30		1000	n.a.	n.a.	0.55				0.310
1000	n.a.		n.a.	0.54	0.310						
1000	n.a.		n.a.	0.55	0.320						
PF40	1400	n.a.	n.a.	0.35	0.580						
	1400	n.a.	n.a.	0.35	0.610						
	1400	n.a.	n.a.	0.36	0.590						
RL15	1400	n.a.	n.a.	0.36	0.590						
	1400	n.a.	n.a.	0.37	0.530						
	1400	n.a.	n.a.	0.36	0.600						
PF40	1400	n.a.	n.a.	0.35	0.560						

Table 1. Cont.

Authors	Binder Type	Additive/Filler	W/b Ratio	Target Density ρ (kg/m ³)	Dry Density ρ (kg/m ³)	Matrix Conductivity (k/W/m)	Dispersed Air Content ϵ	Foaming Agent	Foaming Method	Conductivity Measurement Method	Foam Conductivity (k/W/m)
Wei, S. et al. (2013) [3]	CEMI	FA20	0.40	1900	1870	0.500	0.00	Protein-based	Physical air-entraining	Rapid-K Thermal Conductivity test	0.500
				1700	1636	0.500	0.13				0.423
				1500	1461	0.500	0.22				0.363
				1300	1201	0.500	0.36				0.282
				1000	948	0.500	0.49				0.217
				800	757	0.500	0.60				0.165
				600	570	0.500	0.70				0.124
				500	453	0.500	0.76				0.091
				400	374	0.500	0.80				0.080
				300	252	0.500	0.87				0.065
Mydin, M. (2011) [4]	OPC cement/sand (2:1)	Ref	0.50	650	n.a.	n.a.	0.74	Protein-based	Physical air-entraining	Hot guarded plate test (HGPF)	0.230
				700	n.a.	n.a.	0.71				0.240
				800	n.a.	n.a.	0.64				0.260
				900	n.a.	n.a.	0.57				0.280
				1000	n.a.	n.a.	0.51				0.310
				1100	n.a.	n.a.	0.47				0.340
				1200	n.a.	n.a.	0.44				0.390
				300	364	n.a.	0.77				0.090
				400	510	n.a.	0.70				0.140
				500	563	n.a.	0.64				0.140
Davraz, M. et al. (2016) [5]	CEMI 42.5 R Portland cement	PF/L	0.30	600	715	n.a.	0.58	Protein-based	Physical air-entraining	GHP/HFM-TS EN 12667	0.160
				700	837	n.a.	0.51				0.220
				800	851	n.a.	0.45				0.240
				900	965	n.a.	0.38				0.270
				1000	1100	n.a.	0.32				0.300
				1100	1272	n.a.	0.26				0.320
				1200	1321	n.a.	0.19				0.360
				1300	1429	n.a.	0.13				0.430
				1400	1531	n.a.	0.07				0.500
				1000	975	n.a.	0.53				0.225
Oren, O. H. et al. (2020) [6]	CEM II 42.5R/sand	FA40/Sa	0.91	1000	1029	n.a.	0.51	Protein-based	Physical air-entraining	Transient plane source (TPS)	0.235
				0.55	1000	1033	n.a.				0.50
		FA40/Sa/GBS	0.68	1000	949	n.a.	0.53				0.220
				0.55	1000	1004	n.a.				0.52
		FA40/GBS	0.68	1000	1030	n.a.	0.51				0.230
				0.91	1000	926	n.a.				0.53
		ER0%	0.60	1000	996	n.a.	0.50				0.226
				1000	1132	n.a.	0.49				0.264
				n.a.	n.a.	n.a.	n.a.				0.059
				n.a.	n.a.	n.a.	n.a.				0.064
n.a.	n.a.			n.a.	n.a.	0.063					
n.a.	n.a.			n.a.	n.a.	0.060					
ER3%	0.80	1000	n.a.	n.a.	n.a.	0.063					
		n.a.	n.a.	n.a.	n.a.	0.064					
		n.a.	n.a.	n.a.	n.a.	0.065					
		n.a.	n.a.	n.a.	n.a.	0.069					
		n.a.	n.a.	n.a.	n.a.	0.052					
		n.a.	n.a.	n.a.	n.a.	0.050					
ER6%	0.80	1000	n.a.	n.a.	n.a.	0.054					
		n.a.	n.a.	n.a.	n.a.	0.054					
		n.a.	n.a.	n.a.	n.a.	0.054					
		n.a.	n.a.	n.a.	n.a.	0.053					
		n.a.	n.a.	n.a.	n.a.	0.051					
		n.a.	n.a.	n.a.	n.a.	0.053					
ER9%	1.00	1000	n.a.	n.a.	n.a.	0.051					
		n.a.	n.a.	n.a.	n.a.	0.053					
		n.a.	n.a.	n.a.	n.a.	0.053					
		n.a.	n.a.	n.a.	n.a.	0.053					
		n.a.	n.a.	n.a.	n.a.	0.053					
		n.a.	n.a.	n.a.	n.a.	0.055					
Jiang, J. et al. (2017) [7] (2016) [8]	CEM I 42.5 R Portland cement	Ref	1.00	1000	n.a.	n.a.	0.91	Protein-based	Physical air-entraining	Heat Flow Meter (HFM)	0.053
				1000	n.a.	n.a.	0.91				0.051
				1000	n.a.	n.a.	0.91				0.053
				1000	n.a.	n.a.	0.91				0.053
				1000	n.a.	n.a.	0.91				0.053
				1000	n.a.	n.a.	0.91				0.053
				1000	n.a.	n.a.	0.91				0.053
				1000	n.a.	n.a.	0.91				0.053
				1000	n.a.	n.a.	0.91				0.053
				1000	n.a.	n.a.	0.91				0.053
1000	n.a.	n.a.	0.91	0.053							

Figure 1 provides a plot of the effective conductivity, k_{eff} (W/m/K), as a function of target density (kg/m³), thus summarizing the foams' results with different concentrations of additives and fillers, as collected from experimental datasets. Besides the different types of components and materials employed, Figure 1 depicts a clear increase in the overall thermal conductivity, with an increase in density in all the experiments. The results have been presented in four different foam classes, as described in [75,76]: insulating ultra lightweight (UL) foams having 0–300 kg/m³ density; insulating low-density foams, with 300–800 kg/m³ density; moderate strength foams with 800–1350 kg/m³ density; and structural foams with densities higher than or equal to 1350 kg/m³ density.

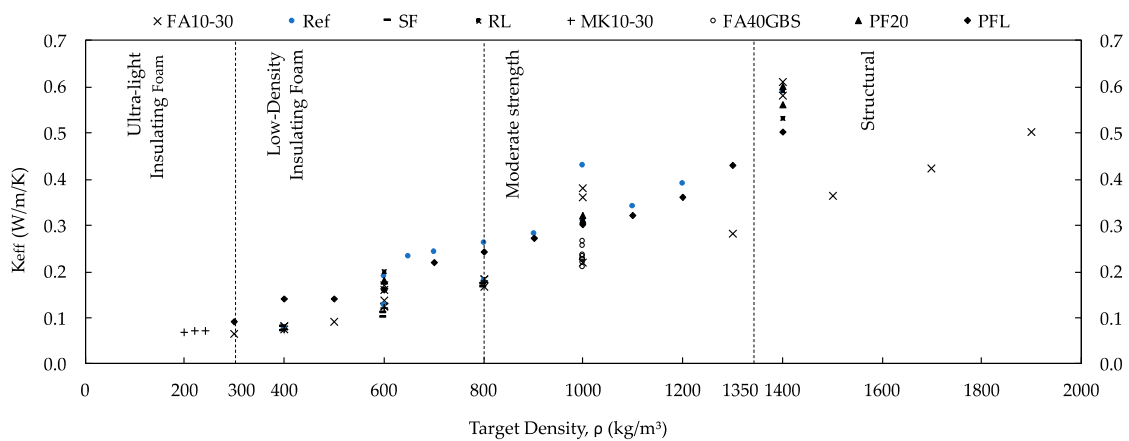


Figure 1. K_{eff} (W/m/K) vs. target density, ρ (kg/m^3) of concrete foams by [67–74]. Ref: Reference foam, FA: Fly ash, SF: Silica fume, RL/L: Limestone, MK: Metakaolin, GBS: Granulated blast furnace slag, PF: Polypropylene fiber.

3. Heat Conduction in Two-Phase Porous System

This section presents a simplified approach for the determination of the homogenized thermal conductivity, k_{eff} (W/m/K) of cementitious foam composites. The model is based on stacked porous amounts (porosity), continuous- and dispersed-phase conductivities, and geometrical classification of pores according to the comprehensive study of the aqueous foam structures presented in [77–79]. The main objective is to propose pore geometrical-fitting parameters that can be employed in designing LHTES/TES-enhanced (two phases) cementitious foams with general low-to-high porosity.

3.1. Modified Lewis-Nielsen Model for Conductivity of Porous Cementitious Composites

Cementitious foam’s microstructure, considered as a two-phase system, can be modelled as a continuous phase made of cement paste (skeleton) and a dispersed phase made of air-voids (Figure 2). The main thermophysical parameters of the two-phase system which govern the homogenized heat transport phenomena include: (i) the specific heat, (ii) the density, (iii) the thermal conductivity (being i., ii., and iii. of the single phases), and (iv) possible thermal lag, i.e., interfaces between these phases. Knowing these parameters, one can describe the thermal behavior of the two-phase porous media.

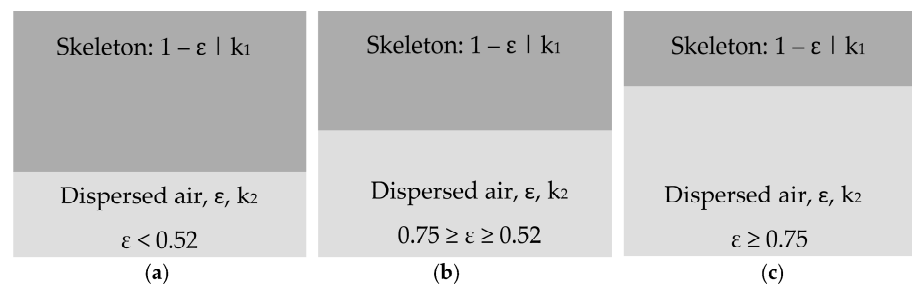


Figure 2. Schematic illustration of a two-phase cementitious foam without considering the meso-scale air-void distribution: (a) low- ($\epsilon < 0.52$), (b) medium- ($0.75 \geq \epsilon \geq 0.52$), and (c) high-porosity ($\epsilon \geq 0.75$).

The thermal conductivity (k) in a two-phase porous system is significantly influenced by the conductivities of the continuous phase (k_1) and the dispersed phase (k_2), and by their concentrations (i.e., $1 - \epsilon$ for the skeleton and ϵ for the dispersed air, as in Figure 2). In this regard, numerous analytical equations have been proposed to solve the effective (i.e., homogenized) thermal conductivity of these two-phase systems. These models are capable of accurately predicting the effective heat transfer by considering and weighting the

porosity and conductivity of each single component. However, these approaches become limited when the pore volume fraction increases and, at the same time, the isolated pores become connected [69]. Nevertheless, the study conducted by Lewis and Nielsen [50,51], while originally based on the theory of the elastic moduli of composite materials, has been found to be a very good approximation for thermal conduction, if enough information about the air content and the pore structure is available.

3.2. Fitting Parameters A and ψ for Porous Cementitious Composites

In this work, the following expression by Lewis and Nielsen [50] has been used as homogenization rule for predicting the conductivity of cementitious foams:

$$\frac{K}{K_1} = \frac{1 + A \frac{K_2/K_1 - 1}{K_2/K_1 + A} \varepsilon}{1 - \frac{K_2/K_1 - 1}{K_2/K_1 + A} \psi \varepsilon} \quad (1)$$

where ε is the fraction of air inclusion, A the shape factor for the dispersed air-voids, and ψ considers the type of packing of the pores, as well as the presence of either predominantly closed or interconnected pores. In Equation (1), the accurate definition (and calibration) of A and ψ represents the key task, one which requires a fundamental knowledge and study of the pore structure of the cementitious foams. For the evolution of A and ψ , it is also important to consider the hydration process and aging time of the foam. Foam pore structures can change during the hardening process due to rheological changes of the cement matrix, with consequent volumetric reduction (shrinkage) of the paste due to drying processes. Also, local failure of individual lamellae at advanced stiffening/solidification time steps can lead to pore systems consisting of intersecting (coalescing) spherical pores. In addition to volume changes, additives with different surface characteristics (polarity) can also influence pore structure developments, leading to uncertainties in pore structure and deviation between the real (measured) and the theoretical (calculated) porosity of the composite.

In the fresh state of the foam, bubble coalescences and/or bubble coarsening are directly related to an increasing of the air inclusion amount, which leads to an increase in the mean pore diameter and a shift of the pore-size distribution towards larger pores. In this regard, pore systems with a predominance of connected pores are formed from polyhedral-shaped foams which have very high air contents ($\varepsilon \geq 0.75$) and exhibit extremely thin lamellae (ca. 20–30 μm). Due to this, highly irregular structures are associated with high-porosity foams with a dwindled cement matrix. In foams with a predominance of spherical bubbles, the minimum and maximum pore sizes, together with their distribution, can influence the maximum achievable porosity. Thus, assuming an ideal distribution of the pore sizes, a geometric maximum-possible porosity of 0.75 can be achieved for foams with spherical bubbles. A classification into polyhedral foams, spherical foams, and bubble systems can be adopted for the characterization of foamed cement pastes. This classification represents a correlation between geometry, fraction of air inclusion (porosity) and bulk density of a fictitious aqueous phase with a bulk density of 2.0 kg/dm^3 [78].

It follows that, by considering the correlation between fraction of air inclusion and void geometry, as sketched in Figure 3, the calibration factors A and ψ can be defined according to the literature. Particularly, the constant A , related to the generalized Einstein coefficient (Einstein, 1905, 1906), which represents primarily the shape of the air inclusions, for any direction of heat flow, can be calculated for aggregates of spheres as [51]:

$$A = \frac{2.5}{\Phi_m} - 1 \quad (2)$$

where Φ_m represents the maximum packing fraction of the randomly dispersed air voids, defined as the true volume of the air voids in cementitious foam divided by the volume they appear to occupy when packed to their maximum extent. In this sense, the three types of foam classes can be taken from Table 2.

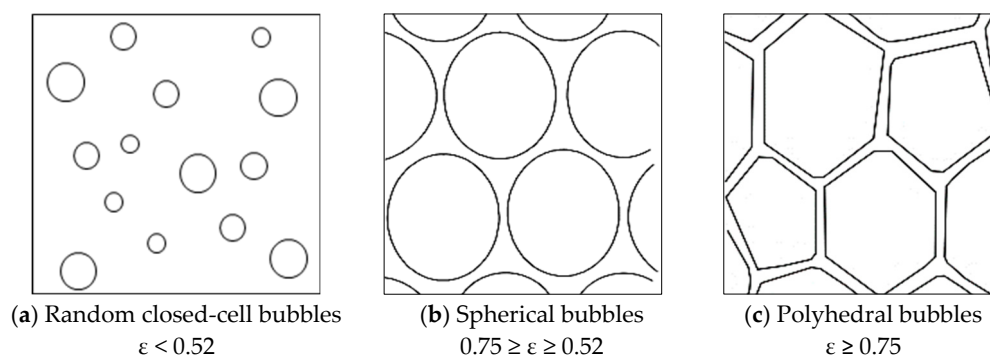


Figure 3. Correlation between the fraction of air inclusion (ϵ) and air void geometry in cementitious foams of (a) low porosity, (b) medium porosity, and (c) high porosity, based on the findings of [77,79].

Table 2. Air-void shape/packing classifications of low-, medium-, and high-porosity cementitious foam; see Supplementary Material S2 for more details.

Air Fraction	Foam Class	Shape of Air Voids	Type of Packing	Maximum Packing Fraction (Φ_m)
$\epsilon \geq 0.75$	I	Polyhedral	Hexagonal close	0.74
$0.75 \geq \epsilon \geq 0.52$	II	Spherical	Random close	0.64
$\epsilon < 0.52$	III	Bubbles	Random loose	0.60

The structural parameter ψ , needed for evaluating the conductivity of cementitious foam, can be estimated as [51]:

$$\psi = 1 + \left(\frac{1 - \Phi_m}{\Phi_m^2} \right) \epsilon \quad (3)$$

In this study, Equations (1)–(3) are employed for predicting the homogenized (effective) conductivity of the analyzed low-to-high porous cementitious foams. The proposed methodological approach enables precise determination of Φ_m (refer to Table 2) for solving Equations (2) and (3) within each foam class, simplifying Equation (1) for enhanced practicality in engineering applications. Consequently, the only remaining unknown parameters are porosity and matrix conductivity. This represents a significant advancement in thermal conductivity assessment, particularly addressing the impact of pore geometry within the mid-to-high-porosity range of mineral foams. This advancement greatly contributes to standardizing the thermal conductivity of mineral foams, enhancing their utility and efficiency in engineering design and applications.

It is important to emphasize that the proposed fitting parameters for mineral foams in this study are based on well-established mathematical principles and exclusively tied to the system's geometry; see Supplementary Material S2 for more details. Determining the correct parameters would be arbitrary and impractical without a comprehensive understanding of the factors influencing thermal conductivity and knowledge of mineral foam pore structures.

4. Analytical Predictions vs. Experimental Data

4.1. Classification of Test Data

In this section, the experimental data presented in Section 2 are analyzed to explore potential correlations between the fraction of air inclusion (ϵ), target density, and effective foam conductivity. The primary aim of this analysis is to classify the data into specific categories, such as low-, medium-, and high-porosity cementitious foams. Additionally, a categorization of the data based on air-void structure/geometry, such as random closed-cell bubbles, spherical bubbles, or polyhedral ones, is considered, as presented in Section 3.2.

This information is crucial for the accurate determination of calibration parameters “A” and “f” in Equation (1).

Figure 4 illustrates the relationship between the fraction of air inclusion (ϵ) and the target density for all datasets [67–74] considered in this study. It demonstrates a consistent linear decrease of porosity with increased density across all the data points. Furthermore, by employing the classification outlined in Section 3.2, the data can be categorized into three distinct foam classes: “Class I” for foams with polyhedral-shaped air voids (exhibiting hexagonal close packing) and a fraction of air inclusion (ϵ) greater than or equal to 0.75; “Class II”, consisting of foams with spherical-shaped bubbles, with random close packing and a fraction of air inclusion ranging from 0.75 to 0.52; lastly, “Class III” are foams with low porosity, with random loose packing and a fraction of air inclusion (ϵ) below 0.52.

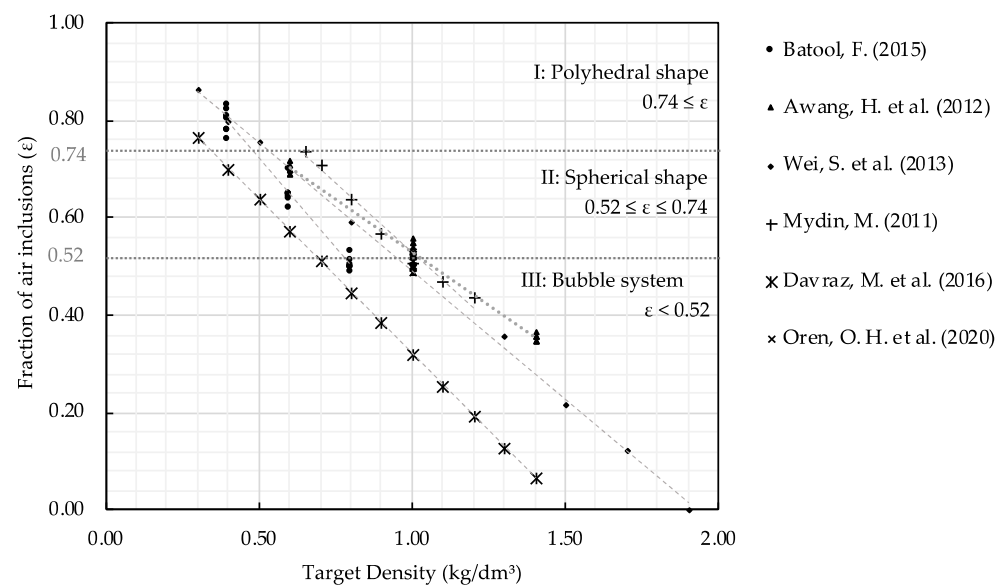


Figure 4. Fraction of air inclusion (ϵ) vs. target density (kg/dm^3); data by [67–74].

Figure 5 displays the correlation between the foams’ homogenized conductivity (k_{eff}) and target density for collected datasets [67–74]. It exhibits a clear linear increase of conductivity against increased density across all the data points. In this case, regarding the presented classification described in Section 2, the data can be categorized into four distinct subtypes: “ultra-light insulating foams”, which possess a target density that is equal to or lower than $0.30 \text{ kg}/\text{dm}^3$; “low-density insulating foams”, which includes foams with target densities ranging from $0.30 \text{ kg}/\text{dm}^3$ to $0.80 \text{ kg}/\text{dm}^3$; “moderate-strength foams”, classifying foams having a target density ranging from $0.80 \text{ kg}/\text{dm}^3$ to $1.35 \text{ kg}/\text{dm}^3$; and finally, “structural foams”, comprising foams with a target density higher than $1.35 \text{ kg}/\text{dm}^3$. It is worth noting that as the density increases, the insulation performance of the material decreases, as indicated by a higher level of foam conductivity.

Figure 6 combines the information from Figures 4 and 5, establishing a correlation between foam effective/homogenized conductivity (k_{eff}) and the fraction of air inclusion (ϵ) for the presented datasets. This graph clarifies the classification of the considered foams, based on air-void structure/geometry and packing characteristics, presenting the related conductivity range (upper and lower values) expected for each foam system class. The classification in Figure 6 identifies three foam classes: the first one consists of foams with bubble types characterized by low porosity and random loose packing ($\epsilon < 0.52$), with expected k_{eff} higher than $0.2 \text{ W}/\text{m}/\text{K}$; the second one comprises foams with predominantly non-connected spherical-shape voids, exhibiting random close packing, and having a fraction of air inclusion ranging from 0.52 to 0.75, with expected k_{eff} between $0.2 \text{ W}/\text{m}/\text{K}$ and $0.1 \text{ W}/\text{m}/\text{K}$; lastly, the third class includes polyhedral-shaped foams, with hexagonal close packing and ϵ greater than or equal to 0.75 with expected k_{eff} less than $0.1 \text{ W}/\text{m}/\text{K}$.

An interesting observation arising from Figure 6 is that the type of internal structure in the foam is directly linked to the total air fraction and the target density of the system.

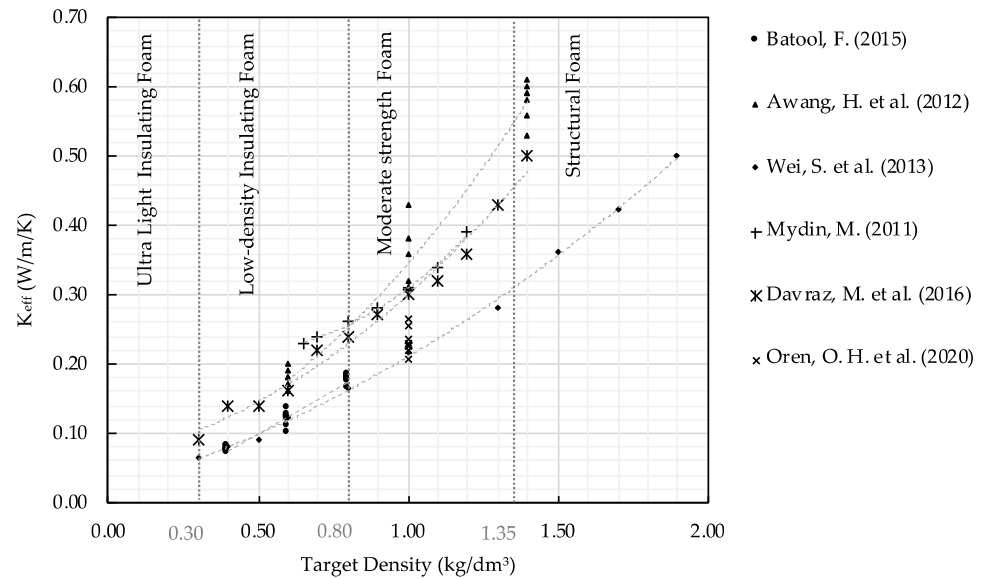


Figure 5. K_{eff} (W/m/K) vs. target density (kg/dm^3); data from [67–74].

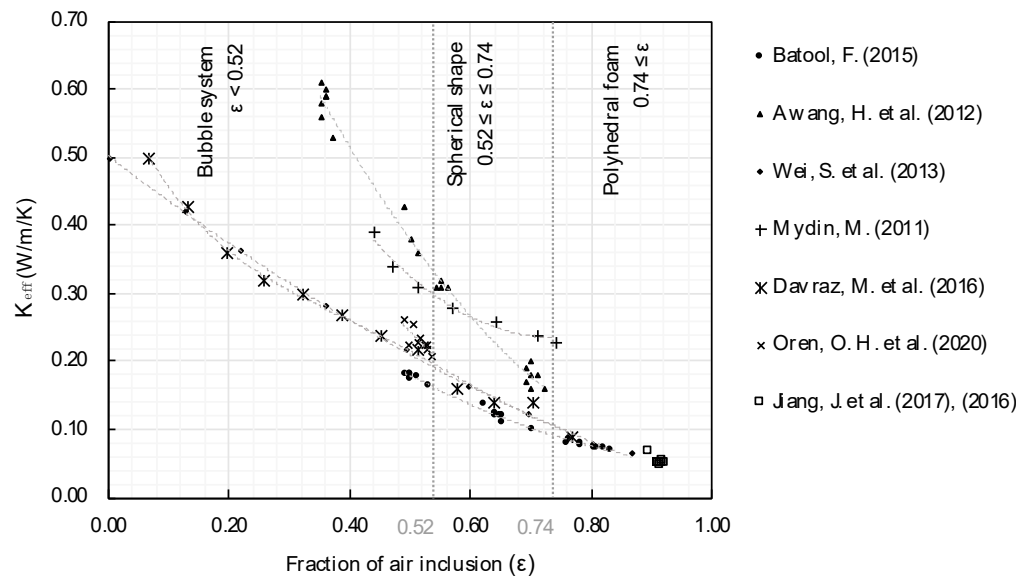


Figure 6. K_{eff} (W/m/K) vs. fraction of air inclusion (ϵ); data by [67–74].

The classifications, as shown between Figures 4–6, are crucial for guiding the subsequent section, which presents a unified approach for modeling heat transfer conductivity in various types of foams. The approach considers a wide range of porosity levels, extending from low to high porosity cementitious foams, and points out the effects of the different types of air-void geometry and meso-structural types. Thus, by understanding the influence of these factors, this section provides valuable insights into the heat-transfer characteristics of mineral foams, enabling a comprehensive understanding of their homogenized thermal conductivity.

4.2. Analytical Description vs. Experimental Measurements of Thermal Conductivity K_{eff}

In this section, the homogenized thermal conductivity of each foam is predicted and compared to the corresponding experimental data from Section 2, as also categorized in

Section 4.1. A total of one hundred foam cases were analyzed, and all the data were unified and calibrated by fitting the parameters “A”, “ Φ_m ”, and “ ψ ”, as listed in Table 3.

Table 3. Calibrated “A”, “ Φ_m ”, and “ ψ ” parameters for the foam concretes determined by [67–74].

Air Fraction	Foam Class	A	Φ_m	ψ
$\varepsilon \geq 0.75$	I	2.37	0.74	1.370
$0.75 \geq \varepsilon \geq 0.52$	II	2.90	0.64	1.563
$\varepsilon < 0.52$	III	3.10	0.60	1.546

The equation (Equation (1)) used for the analysis is modified, as:

$$\frac{K}{K_1} = \frac{1 + A \frac{K_2/K_1 - 1}{K_2/K_1 + A} \varepsilon}{1 - \frac{K_2/K_1 - 1}{K_2/K_1 + A} \left(1 + \left(\frac{1 - \Phi_m}{\Phi_m^2}\right) \varepsilon\right) \varepsilon} \quad (4)$$

Figure 7 illustrates all the data in terms of effective thermal conductivity (k_{eff}), based on the data from [67–74], and the predicted values obtained using the modified Lewis–Nielsen expression proposed in Equation (4).

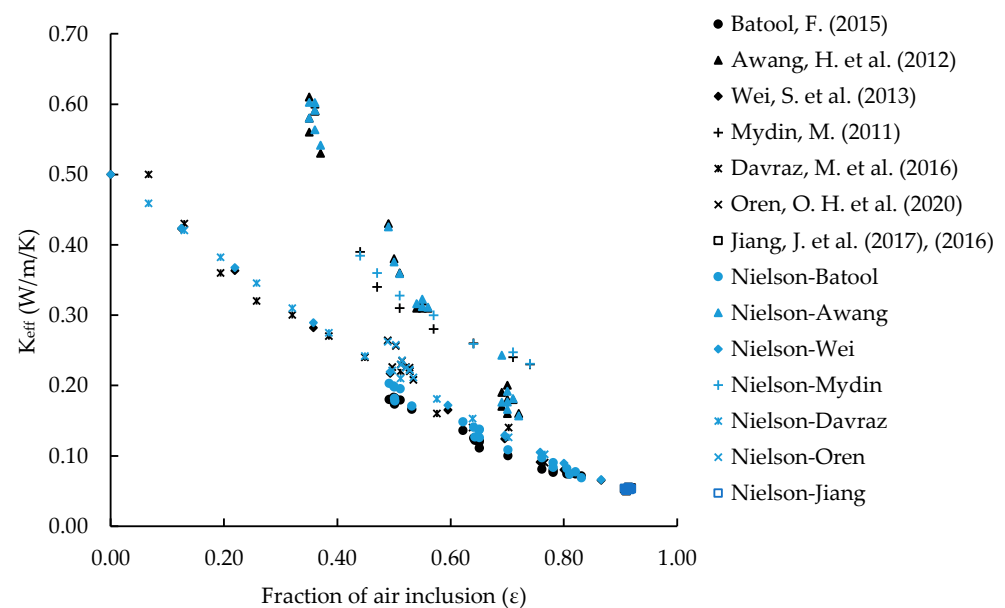


Figure 7. K_{eff} (W/m/K) [67–74] vs. fraction of air inclusion (ε); blue points indicate the predicted values and black points indicate the experimental findings.

Notably, the homogenized conductivity predictions can be achieved by solely calibrating “A” and “ Φ_m ” parameters, which are mainly influenced within the three distinct foam classes mentioned in Section 3.2. Specifically, the fundamental factors are the foam air-volume fraction and the dispersed air-geometry characteristics, while one can disregard other factors, such as binder variations, casting types, foaming agents, and other components/amounts. This aspect represents the significant contribution of this study, as the application of the modified Lewis–Nielsen expression to an extensive dataset of mineral foams with widely scattered formulations and thermal responses has not been attempted previously. This limitation arises from the lack of sufficient experimental data regarding the classification of pore geometry in mineral foams, a crucial factor for determining the appropriate values of parameters A and Φ_m in model implementation.

The presented results show that, by considering the shape of the dispersed air and their packing characteristics, a consistent stable response for each foam type can be achieved, i.e., class I (polyhedral-shaped air voids), class II (spherical-shaped), and class III foams

(loosely packed bubble inclusion). There is substantial good agreement between the theory and the experimental data.

To demonstrate the effectiveness of this approach, Figure 8 shows the homogenized predicted conductivity values plotted against the employed data. The figure displays both the linear-regression curve and the square-root error, both of which help to identify the best-fit line that presents the relationship between the measured variables and the predicted ones.

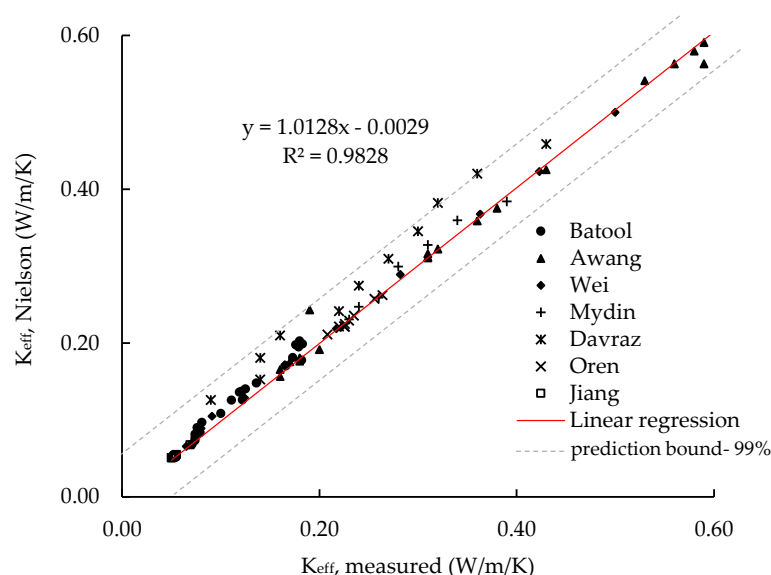


Figure 8. Lewis-Nielsen predictions: k_{eff} , Nielson (W/m/K) vs. measured conductivity k_{eff} , measured (W/m/K), for all collected data; comparison and linear regression + R^2 , slope >1 model overestimates the conductivity data.

The prediction results reveal promising outcomes, with a high R^2 value of 0.9828 and a regression line slope of 1.0128. In Supplementary Material S3, Figures S2–S8 show the homogenized predicted conductivity values plotted against the employed data, analyzed author by author. The agreement between experimental values and predicted ones is remarkable; see Figure 8. A prediction interval, within which, with a probability of 99%, future observations are expected to fall, is presented in Figure 8. It provides an uncertainty of 0.02 W/m/K surrounding the predicted foam homogenized conductivity value by applying the proposed approach. The scatter in the data can potentially be attributed to the experimental errors due to sampling, measurement techniques, and measurement accuracy.

It is possible to further simplify and extend Equation (4) by incorporating the parameters from Table 3. However, the predictive results obtained demonstrated remarkable accuracy, closely matching the experimental data. At this point, there is no compelling reason to extend the equation further.

4.3. Extension of the Analytical Model for Porous LHTES-Systems (Mineral Foams)

The main objective of the analytical model proposed in Sections 4.1 and 4.2 was to predict the conductivity, or the homogenized one, of cementitious foams made of various types and amounts of components and having variable properties. By knowing the conductivity of the matrix (or skeleton) and considering the amount of air inclusion (porosity), and by using the analytical formula based on air dispersion shape and packing, the conductivity of the homogenized porous system was well predicted.

Based on this, now the model can be extended to predict the conductivity of latent-heat-storage-enhanced porous systems. The goal is to facilitate simulations through simple engineering calculations, without the need to perform expensive experimental tests. The estimation of the homogenized conductivity of LHTES-enhanced foams is thus considered

by employing different optimization methods, such as embedding microencapsulated phase change material (MPCM) within the skeleton at various percentages (i.e., 10%, 20%, 30%, and 40%). The investigation is limited to 40%, since higher percentages have been found to compromise foam stability. The proposed analytical formula (Equation (4)) has been employed by adopting the parameters of the LHTES-enhanced skeleton (MPCM pastes) by Sam et al. [80], including the thermal conductivity data for the MPCM paste, in both liquid and solid phases. The conductivity of the air is sourced from the literature. All these data are summarized in Table 4.

Table 4. Data used in the proposed model to predict homogenized conductivity of thermal-energy-storage mineral foam composites; see Sam et al. [80].

	Vol.- %MPCM in Paste	K_{eff} Paste (w/b = 0.4) Solid Phase MPCM (W/m/K)	K_{eff} Paste (w/b = 0.4) Liquid Phase MPCM (W/m/K)
LHTES Paste	40	0.600	0.464
	20	0.754	0.759
K_{eff} Ref Paste (W/m/K)		0.89–0.93	
K Air(W/m/K)		0.025	

The graphs of Figures 9 and 10 illustrate the predicted homogenized conductivities of the LHTES/TES-enhanced foams, with and without considering 20% and 40% of MPCM pastes in comparison.

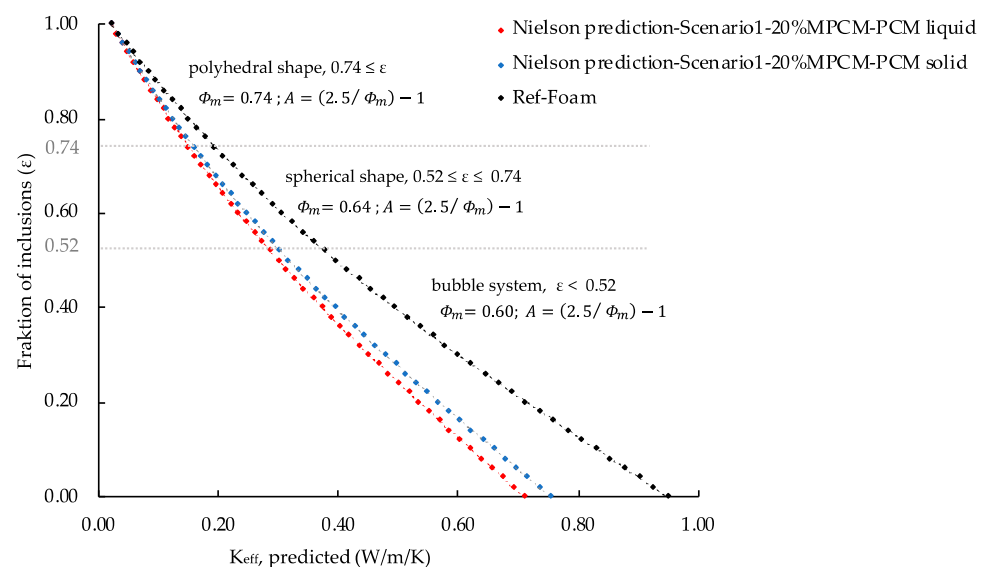


Figure 9. Foam with skeleton having 0% (Ref) and 20% MPCM: fraction of air inclusion (ϵ) vs. k_{eff} , predicted (W/m/K).

More specifically, the skeleton of the foams consists of cement paste with a water-to-binder ratio of 0.40, which was mixed with a commercial MPCM having a melting/solidification temperature of 24 °C, with volume percentage substitutions of 0%, 20% and 40%, respectively. The experimental data were tested by the author in the previous work; see Sam et al. [80]. By analyzing the graphs, the conductivity range within each foam class and porosity level can be determined at any desired porosity. The effective homogenized values for 10% and 30% of MPCM substitutions in the paste can be smoothly interpolated from the data available in this section.

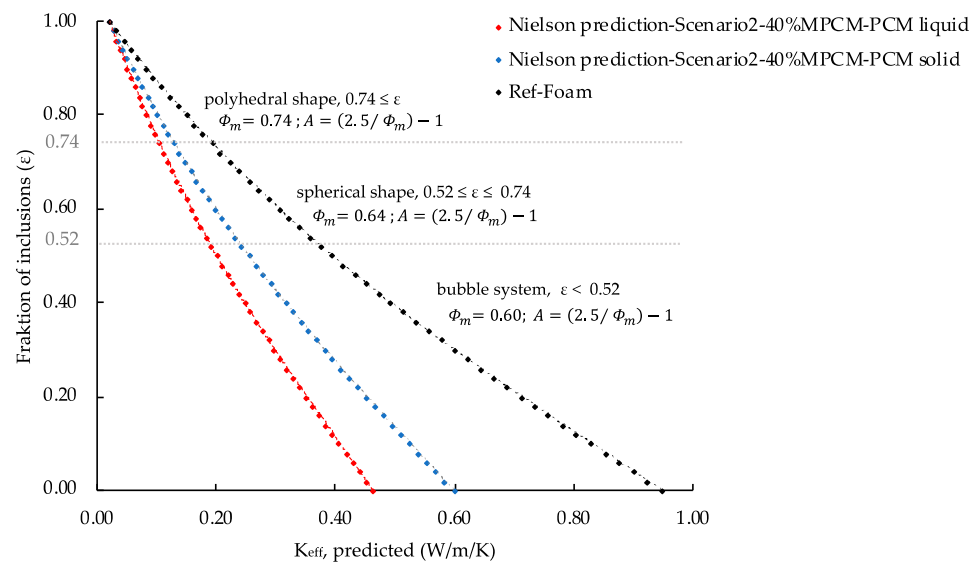


Figure 10. Foam with skeleton having 0% (Ref) and 40% MPCM: fraction of air inclusion (ϵ) vs. k_{eff} , predicted (W/m/K).

In conclusion, Table 5 presents the predicted homogenized conductivity ranges for different foam classes and volumetric amounts of MPCM, offering insights into the conductivity of polyhedral and spherical foam systems (of both Class I and II) with porosities higher than 52%, which can be used for energy storage purposes.

Table 5. Proposed predicted conductivity range for further thermal analysis and numerical simulations. Values for specific porosity can be taken from Figures 9 and 10.

	Foam Class	Vol-%MPCM in Paste	k_{eff} Foam Solid Phase PCM (W/m/K)	k_{eff} Foam Liquid Phase PCM (W/m/K)
TES Polyhedral Foam	I	40	≤ 0.14	≤ 0.10
		20	≤ 0.17	≤ 0.15
TES Spherical Foam	II	40	≤ 0.24	≤ 0.20
		20	≤ 0.30	≤ 0.28
TES Polyhedral Foam	I	0	≤ 0.2	
TES Spherical Foam	II	0	≤ 0.39	

This information is utilized for a 1D-wall simulation presented next, in Section 5, by incorporating porosity and effective thermal conductivity of TES-Foam with and without MPCM.

5. Integration of LHTES and Dynamic Envelopes: Application Scenario-1D Model Based on the First Law of Thermodynamics

In this section, the thermal performance of multi-layer enclosing structures consisting of expanded polystyrene (EPS) and TES-foam (foam having porosity higher than 52%) as external layers and reinforced concrete as main structural layer is assessed by using standard one-dimensional (1D) FEM simulation. More details about the applied theoretical background are presented in Supplementary Materials S4.

This chapter underscores the model’s physical significance for a building envelope and illustrates how the model simplifies the intricate numerical calculations that were previously required to determine the thermal conductivity of mineral foams. These calculations include scenarios involving 20% MPCM in the skeleton and 90% porosity.

The analytical model implemented enables the straightforward representation of thermal behavior within building envelopes by the modification of input parameters such

as matrix conductivity and/or porosity. This analytical capability extends to the calculation and implementation of conductivity while addressing concerns related to volumetric heat capacity through a simple one-dimensional FEM simulation.

Parametric Studies for Thermal Performance in Multi-Layer Structures (EPS vs. TES Foam Composites)

The heat flow via conduction through a two-layer enclosing structure is schematized in Figure 11: the x -axis denotes the direction of the one-dimensional heat flux, and considers a heat flow between the exterior layer, L1 (0.1 m thickness), and the interior one, L2 (0.2 m thickness), with total thickness of $\Delta x = 0.3$ m.

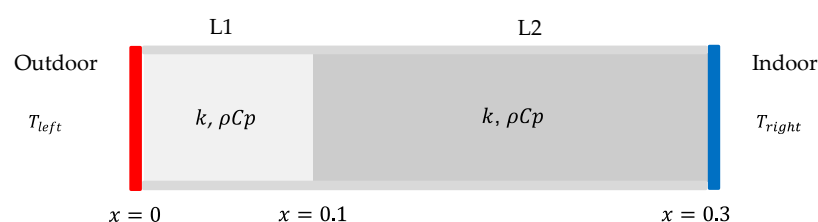


Figure 11. Schematized one-dimensional (1D) conduction model for a two-layer wall.

For one-dimensional heat flow, the temperature gradient through the structure is simulated. To solve the heat transfer problem (as shown in the Supplementary Materials), two nodes' truss finite elements (FEs) were adopted and the non-linear FEM problem was solved in MATLAB; the space discretization of the wallboard uses 100 FEs, while for the temporal one, an implicit backward Euler method with a time stepping of 5 min within 24 h was chosen. Initial boundary conditions considered an initial temperature $T_0 = 20$ °C (i.e., at $t = 0$), while essential (Dirichlet types) boundary conditions were fixed according to two case studies:

- "Summer" $T(x = 0, t) = T_{left} = 40$ °C $T(x = 0.3, t) = T_{right} = 20$ °C;
- "Winter" $T(x = 0, t) = T_{left} = -5$ °C $T(x = 0.3, t) = T_{right} = 20$ °C;

Two scenarios are simulated: wall section with TES-foam as insulating layer L1 containing 2% MPCM (T_m : 24); and wall section with EPS as insulating layer L1. Tables 6 and 7 provide the key thermophysical parameters of the considered EPS and TES foam with and without MPCM for the analysis of the thermal behavior of the two-layer wall sections.

Table 6. Thermophysical properties of single components relevant for calculating the volumetric heat capacity of TES foam, both with and without MPCM, using mixture theory.

	Paste [80]	Air	MPCM [80]
Density, ρ (kg/m ³)	1708	1.2	760
Sensible heat capacity, C_p (J/kg/K)	1300	1000	2100
Latent heat storage, h (kJ/kg)	0	0	195

Table 7. Thermophysical properties of composites: model input for simulating one-dimensional (1D) temperature profiles. 'TES-Foam' denotes foam with porosity higher than 52% and without integrated MPCM. * Foam with $\epsilon = 0.90$, MPCM in solid phase.

	TES-Foam 0% MPCM	TES-Foam 2% MPCM	RC-Wall	EPS [81,82]
Density, ρ (kg/m ³)	200	90	2000	30
Predicted effective conductivity, k_{eff} (W/m/K)	0.07 *	0.05 *	2.1	0.04
Volumetric heat capacity, C_p , sensible (kJ/m ³ /K)	223.120	210.632	1760	45
Latent heat storage, h (kJ/m ³)	0	2964	0	0

Using the measured thermophysical properties of single components shown in Table 6, the volumetric heat capacity of TES-foam with and without MPCM can be simply ascertained by applying the mixture law [61]; see Table 7. Density and effective conductivity of TES-foams with 90% porosity are two parameters derived from the presented model in Sections 3 and 4.

Figures 12 and 13 present the transient temperature distribution along the x direction across the two-layer structure, showing the differing responses of EPS and TES-Foam with 2% volumetric amount of MPCM to the heat and cold wave. The initial scenario involves both outside and inside temperatures equal to 20 °C at t_0 . Subsequently, a sudden increase/decrease in the outside temperature to 40 °C/−5 °C occurs. The graphs depict the temperature distribution inside the wall at 5 min intervals. In both Figures 12 and 13, T_1 represents the temperature at location x_1 , recorded 5 min after the initiation of a temperature increase or decrease, demonstrating a noticeably slower rate of temperature change in response to both heat (Figure 12) and cold (Figure 13) wave stimuli for TES-Foam.

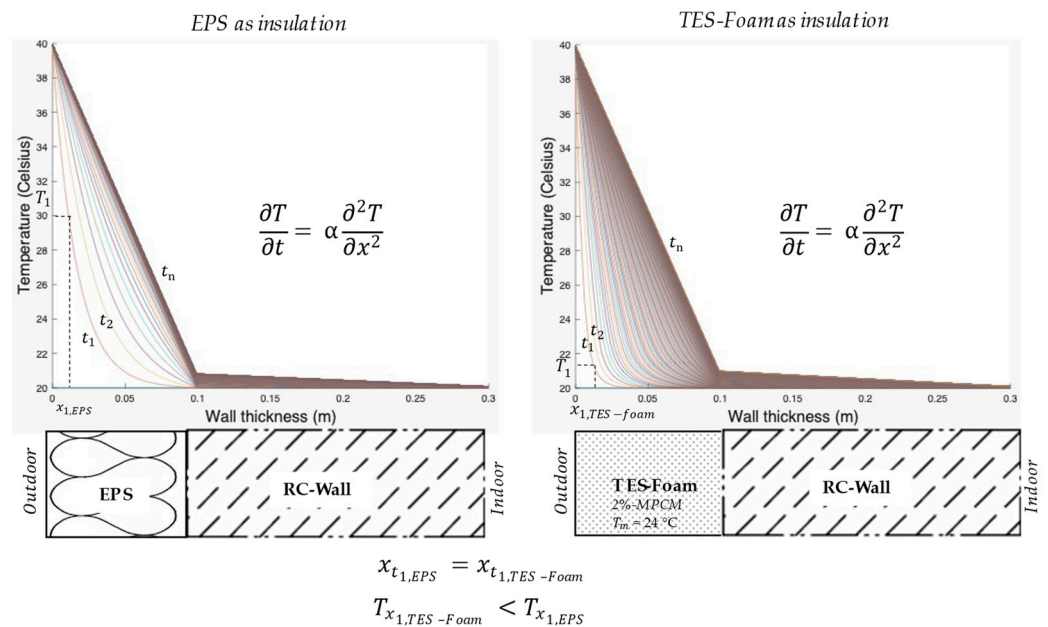


Figure 12. One-dimensional (1D) transient temperature field across the wall with thickness ($\Delta x = 30$ cm), at t_0 , the temperature difference $\Delta T = 0$ ($T_{\text{inside}} = T_{\text{outside}} = 20$); sudden outside temperature increase to $T_{\text{outside}} = 40$ to evaluate the wall response to heat wave at any fixed position along the x axis. The temperature profile for the wall section is depicted using lines of different colors at various time intervals: $t_1 = 5$ min, $t_2 = 10$ min, up to $t_n = 24$ h.

The simulation results shown in Figures 12 and 13 indicate that the volumetric heat capacities of the materials have a decisive impact on the capacity of heat storage and prolonging the heat/cold penetration, providing a balanced and energy-efficient means of maintaining indoor comfort. A significantly higher volumetric heat capacity of TES/LHTES-Foam ($223.120 \text{ kJ/m}^3/\text{K}/210.632 \text{ kJ/m}^3/\text{K}$) in comparison to EPS ($45 \text{ kJ/m}^3/\text{K}$) reduces the required storage volume and, at the same time, the structure thickness.

TES-Foam functions as thermal mass or thermal battery, effectively moderating internal temperatures by mitigating day–night temperature fluctuations. When integrated as LHTES-Foam, TES-Foam significantly enhances its thermal capacity through the efficient latent heat storage and controlled release of heat energy. During warmer periods, it adeptly absorbs and stores excess heat, while during cooler periods, it steadily releases the stored heat, contributing to the stabilization and regulation of indoor temperatures. This dual functionality of TES Foam as both a thermal mass and an advanced LHTES material provides a robust and energy-efficient solution for maintaining a consistently comfortable indoor environment, regardless of external weather variations.

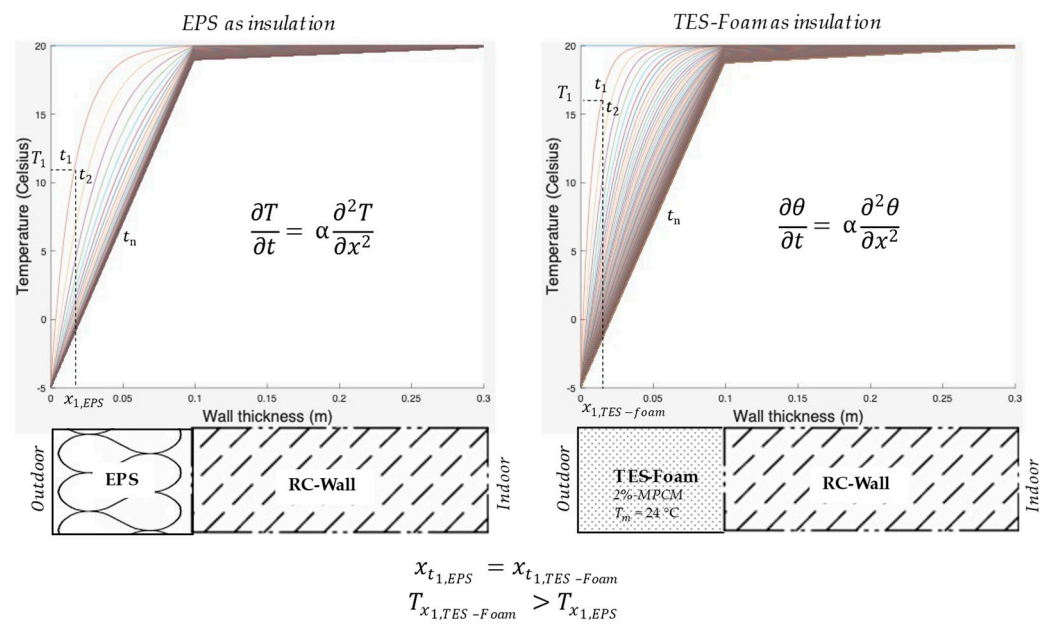


Figure 13. One-dimensional (1D) transient temperature field across the wall with thickness ($\Delta x = 30$ cm), at t_0 , the temperature difference $\Delta T = 0$ ($T_{\text{inside}} = T_{\text{outside}} = 20$); sudden outside temperature decrease to $T_{\text{outside}} = -5$ to evaluate the wall’s response to a cold wave at any fixed position along the x axis. The temperature profile in the wall section is depicted using lines of different colors at various time intervals: $t_1 = 5$ min, $t_2 = 10$ min, up to $t_n = 24$ h.

Table 8 summarizes the calculated thermal diffusivity (α) and thermal effusivity (b) variables of proposed structures to assess the thermal performance under transient boundary conditions and conducts an evaluation of the energy-saving capacities of both structures. Lower thermal diffusivity of LHTES/ TES-Foam ($0.0237 \cdot 10^{-5} \text{ m}^2/\text{s}$ / $0.0314 \text{ m}^2/\text{s}$), compared to EPS ($0.08 \cdot 10^{-5} \text{ m}^2/\text{s}$), provides a much slower response to temperature differences, and decreases the transient heat transfer, or the progression of a temperature wave in the system, extending the time for charging and discharging of heat/cold load and turns, all in a more thermally inert system; also see Figures 12 and 13. This is especially beneficial for reducing over-temperature degree hours in indoor spaces. A much higher thermal effusivity value for LHTES/ TES-Foam ($102.6 \text{ m}^2/\text{k}/\text{S}^{0.5}$ / $124.9 \text{ m}^2/\text{k}/\text{S}^{0.5}$ vs. $42.5 \text{ m}^2/\text{k}/\text{S}^{0.5}$ for EPS) leads to a larger amount of heat being stored, which is significant for the effectiveness of internal storage masses.

Table 8. Calculated thermophysical properties relevant for dynamic envelope evaluation; thermal diffusivity $\alpha = \lambda/\rho c_p$ and heat penetration coefficient $b = \sqrt{\lambda \rho c_p}$.

	TES-Foam 0% MPCM	TES-Foam 2% MPCM	RC- Wall	EPS
Thermal diffusivity, $\alpha \cdot 10^{-5} (\text{m}^2/\text{S})$	0.0314	0.0237	0.15	0.08
Heat penetration coefficient, $b (\text{J}/(\text{m}^2/\text{k}/\text{S}^{0.5}))$	124.9	102.6	1922.5	42.5

6. Conclusions

This paper presents an analytically based approach which combines the effective thermal conductivity of the foam skeleton with dispersed air bubbles, creating a porous media system. The objective is to provide a comprehensive description and precise prediction of the thermal behavior of TES-mineral foams with/without LHTES (incorporation of MPCM), with varying porosity levels, ranging from low to high, with the final goal of facilitating simulations through simple engineering calculations, and without the need to perform expensive experimental tests.

Considering the correlation between porosity and geometry of the dispersed air, through the porous mineral systems, six fitting values of parameters “A” and “ Φ_m ” were proposed for use in the modified analytical expression proposed by Lewis and Nielsen (1940), based on three distinct foam classes: Class I foams, having polyhedral-shaped air voids and a fraction of air inclusion (ϵ) greater than or equal to 0.75; Class II foams, having spherical-shaped bubbles and a fraction of air inclusion ranging from 0.75 to 0.52; and lastly, Class III foams, with low porosity and a fraction of air inclusion (ϵ) below 0.52. The calculated homogenized conductivities were validated by using the proposed fitting parameters and upon the collected experimental data, resulting in a consistently stable response for all foam classes and datasets.

By determining the effective conductivity of TES-mineral foams, with and without latent heat integration, at high porosity of 90%, and by calculating the volumetric heat capacity of the composite using the mixture theory, the potential of LHTES/ TES-enhanced mineral foams to be used for thermal energy storage purposes was discussed. In this regard, thermal diffusivity and the heat penetration coefficient of the LHTES/ TES-enhanced mineral foams was calculated and compared with conventional EPS. The results showed a 3.5 to 4 times higher value for thermal storage capacity and an almost 70%/60% lower thermal diffusivity for LHTES/ TES-enhanced mineral foams, respectively, compared to EPS layers, without considering the latent heat storage amount (h).

Future research directions might aim at exploring new building envelopes that incorporate dynamic thermal performance. This approach differs from conventional solutions, which are based on obsolete concepts of insulation and thermal resistance (R-value) parameters. The main goal will be to synergistically integrate both insulation materials and latent heat thermal storage (LHTS), thus opening new perspectives for prospective novel envelope designs. Research studies regarding their long-term stability, durability, and performance under different environmental conditions would contribute to a comprehensive understanding of their applicability in real-world scenarios.

Supplementary Materials: The following supporting information can be downloaded at: <https://www.mdpi.com/article/10.3390/en16186687/s1>.

Author Contributions: Conceptualization, M.N.S.; Methodology, M.N.S.; Validation, M.N.S.; Formal analysis, M.N.S.; Investigation, M.N.S.; Data curation, M.N.S.; Writing—original draft, M.N.S.; Writing—review & editing, M.N.S., J.S. and H.V.L.; Visualization, M.N.S.; Supervision, J.S. and H.V.L.; Funding acquisition, J.S. and H.V.L. All authors have read and agreed to the published version of the manuscript.

Funding: We acknowledge support by the Deutsche Forschungsgemeinschaft (DFG, German Research Foundation) and the Open Access Publishing Fund of Technical University of Darmstadt.

Data Availability Statement: The data that support the findings of this study are available in Supplementary Materials. Further data are available from the authors upon reasonable request.

Conflicts of Interest: The authors declare that they have no known competing financial interest or personal relationships that could have appeared to influence the work reported in this paper.

References

1. Miller, S.A.; Habert, G.; Myers, R.J.; Harvey, J.T. Achieving net zero greenhouse gas emissions in the cement industry via value chain mitigation strategies. *One Earth* **2021**, *4*, 1398–1411. [[CrossRef](#)]
2. Chen, X.-S.; Li, Y.-P.; Jiang, Y.-L.; Liu, Y.-X.; Zhang, T. Theoretical research on gas seepage in the formations surrounding bedded gas storage salt cavern. *Pet. Sci.* **2022**, *19*, 1766–1778. [[CrossRef](#)]
3. Xue, W.; Wang, Y.; Chen, Z.; Liu, H. An integrated model with stable numerical methods for fractured underground gas storage. *J. Clean. Prod.* **2023**, *393*, 136268. [[CrossRef](#)]
4. Yang, T.; King, W.P.; Miljkovic, N. Phase change material-based thermal energy storage. *Cell Rep. Phys. Sci.* **2021**, *2*. [[CrossRef](#)]
5. Lu, S.; Lin, Q.; Liu, Y.; Yue, L.; Wang, R. Study on thermal performance improvement technology of latent heat thermal energy storage for building heating. *Appl. Energy* **2022**, *323*, 119594. [[CrossRef](#)]

6. Hassan, F.; Jamil, F.; Hussain, A.; Ali, H.M.; Janjua, M.M.; Khushnood, S.; Farhan, M.; Altaf, K.; Said, Z.; Li, C. Recent advancements in latent heat phase change materials and their applications for thermal energy storage and buildings: A state of the art review. *Sustain. Energy Technol. Assess.* **2021**, *49*, 101646. [CrossRef]
7. Heim, D.; Pawłowski, M. The methodology of thermal energy management for nearly zero energy buildings. *Period. Polytech. Civ. Eng.* **2019**, *63*, 499–517. [CrossRef]
8. Al-Yasiri, Q.; Szabó, M. Experimental study of PCM-enhanced building envelope towards energy-saving and decarbonisation in a severe hot climate. *Energy Build.* **2023**, *279*, 112680. [CrossRef]
9. Piselli, C.; Prabhakar, M.; de Gracia, A.; Saffari, M.; Pisello, A.L.; Cabeza, L.F. Optimal control of natural ventilation as passive cooling strategy for improving the energy performance of building envelope with PCM integration. *Renew. Energy* **2020**, *162*, 171–181. [CrossRef]
10. Saffari, M.; de Gracia, A.; Fernández, C.; Cabeza, L.F. Simulation-based optimization of PCM melting temperature to improve the energy performance in buildings. *Appl. Energy* **2017**, *202*, 420–434. [CrossRef]
11. Park, J.H.; Berardi, U.; Chang, S.J.; Wi, S.; Kang, Y.; Kim, S. Energy retrofit of PCM-applied apartment buildings considering building orientation and height. *Energy* **2021**, *222*, 119877. [CrossRef]
12. Ryms, M.; Klugmann-Radziemska, E. Possibilities and benefits of a new method of modifying conventional building materials with phase-change materials (PCMs). *Constr. Build. Mater.* **2019**, *211*, 1013–1024. [CrossRef]
13. Marani, A.; Nehdi, M.L. Integrating phase change materials in construction materials: Critical review. *Constr. Build. Mater.* **2019**, *217*, 36–49. [CrossRef]
14. Chihab, Y.; Bouferra, R.; Garoum, M.; Essaleh, M.; Laaroussi, N. Thermal inertia and energy efficiency enhancements of hollow clay bricks integrated with phase change materials. *J. Build. Eng.* **2022**, *53*, 104569. [CrossRef]
15. Sawadogo, M.; Duquesne, M.; Belarbi, R.; Hamami, A.E.A.; Godin, A. Review on the integration of phase change materials in building envelopes for passive latent heat storage. *Appl. Sci.* **2021**, *11*, 9305. [CrossRef]
16. Ben Romdhane, S.; Amamou, A.; Ben Khalifa, R.; Saïd, N.M.; Younsi, Z.; Jemni, A. A review on thermal energy storage using phase change materials in passive building applications. *J. Build. Eng.* **2020**, *32*, 101563. [CrossRef]
17. Ascione, F.; Bianco, N.; De Masi, R.F.; de' Rossi, F.; Vanoli, G.P. Energy refurbishment of existing buildings through the use of phase change materials: Energy savings and indoor comfort in the cooling season. *Appl. Energy* **2014**, *113*, 990–1007. [CrossRef]
18. Du, K.; Calautit, J.; Wang, Z.; Wu, Y.; Liu, H. A review of the applications of phase change materials in cooling, heating and power generation in different temperature ranges. *Appl. Energy* **2018**, *220*, 242–273. [CrossRef]
19. Drissi, S.; Mo, K.H.; Falchetto, A.C.; Ling, T.-C. Understanding the compressive strength degradation mechanism of cement-paste incorporating phase change material. *Cem. Concr. Compos.* **2021**, *124*, 104249. [CrossRef]
20. Bao, X.; Tian, Y.; Yuan, L.; Cui, H.; Tang, W.; Fung, W.; Qi, H. Development of high performance PCM cement composites for passive solar buildings. *Energy Build.* **2019**, *194*, 33–45. [CrossRef]
21. Kishore, R.A.; Bianchi, M.V.; Booten, C.; Vidal, J.; Jackson, R. Optimizing PCM-integrated walls for potential energy savings in U.S. Buildings. *Energy Build.* **2020**, *226*, 110355. [CrossRef]
22. Yang, Y.K.; Kim, M.Y.; Chung, M.H.; Park, J.C. PCM cool roof systems for mitigating urban heat island—An experimental and numerical analysis. *Energy Build.* **2019**, *205*, 109537. [CrossRef]
23. Abouebeid, S.; Hany, N.; Mosaad, G. Towards enhancing indoor environmental quality: A case of smart adaptive building envelopes in a coastal city. *F1000Research* **2022**, *11*, 731. [CrossRef]
24. Marszal-Pomianowska, A.J.; Johra, H.; Madsen, H.; Kazmi, H.S.; Knotzer, A.; Salom, J.; Lopes, R. Principles of Energy Flexible Buildings: Energy in Buildings and Communities Programme. 2020. Available online: <https://www.annex67.org/media/1918/principles-of-energy-flexible-buildings.pdf> (accessed on 15 August 2023).
25. Hekimoğlu, G.; Nas, M.; Ouikhalfan, M.; Sari, A.; Tyagi, V.; Sharma, R.; Kurbetci, S.; Saleh, T.A. Silica fume/capric acid-stearic acid PCM included-cementitious composite for thermal controlling of buildings: Thermal energy storage and mechanical properties. *Energy* **2020**, *219*, 119588. [CrossRef]
26. Cabeza, L.F.; Navarro, L.; Pisello, A.L.; Olivieri, L.; Bartolomé, C.; Sánchez, J.; Álvarez, S.; Tenorio, J.A. Behaviour of a concrete wall containing micro-encapsulated PCM after a decade of its construction. *Sol. Energy* **2020**, *200*, 108–113. [CrossRef]
27. Omrany, H.; Chang, R.; Soebarto, V.; Zhang, Y.; Ghaffarianhoseini, A.; Zuo, J. A bibliometric review of net zero energy building research 1995–2022. *Energy Build.* **2022**, *262*, 111996. [CrossRef]
28. Posani, M.; Veiga, M.D.R.; de Freitas, V.P. Towards resilience and sustainability for historic buildings: A review of envelope retrofit possibilities and a discussion on hygric compatibility of thermal insulations. *Thermal Insulations. Int. J. Arch. Heritage* **2019**, *15*, 807–823. [CrossRef]
29. Gilka-Böttzow, A.; Folino, P.; Maier, A.; Koenders, E.A.B.; Caggiano, A. Triaxial failure behavior of highly porous cementitious foams used as heat insulation. *Processes* **2021**, *9*, 1373. [CrossRef]
30. Vaou, V.; Pnias, D. Thermal insulating foamy geopolymers from perlite. *Miner. Eng.* **2010**, *23*, 1146–1151. [CrossRef]
31. Modesti, M.; Lorenzetti, A.; Besco, S. Influence of nanofillers on thermal insulating properties of polyurethane nanocomposites foams. *Polym. Eng. Sci.* **2007**, *47*, 1351–1358. [CrossRef]
32. Gonçalves, M.C.; Margarido, F. *Materials for Construction and Civil Engineering*; Springer: Cham, Switzerland, 2015.
33. Arzumanyan, A. Technological peculiarities of non autoclaved foam concrete production on the base of volcanic pumice aggregates. In *Materials Science. Mater. Sci. Forum* **2019**, *974*, 206–210. [CrossRef]

34. Puga, H.; Carneiro, V.; Jesus, C.; Pereira, J.; Lopes, V. Influence of particle diameter in mechanical performance of Al expanded clay syntactic foams. *Compos. Struct.* **2018**, *184*, 698–703. [[CrossRef](#)]
35. Gao, H.; Liu, H.; Liao, L.; Mei, L.; Lv, G.; Liang, L.; Zhu, G.; Wang, Z.; Huang, D. Improvement of performance of foam perlite thermal insulation material by the design of a triple-hierarchical porous structure. *Energy Build.* **2019**, *200*, 21–30. [[CrossRef](#)]
36. Rugele, K.; Lehmus, D.; Hussainova, I.; Peculevica, J.; Lisnanskis, M.; Shishkin, A. Effect of fly-ash cenospheres on properties of clay-ceramic syntactic foams. *Materials* **2017**, *10*, 828. [[CrossRef](#)] [[PubMed](#)]
37. Shishkin, A.; Bumanis, G.; Irtiseva, K.; Ozolins, J.; Korjamins, A. Clay Ceramic Hollow Sphere—Cement Syntactic Foam Composite for Building Applications. *Key Eng. Mater.* **2019**, *800*, 228–234. [[CrossRef](#)]
38. Fernando, P.; Jayasinghe, M.; Jayasinghe, C. Structural feasibility of Expanded Polystyrene (EPS) based lightweight concrete sandwich wall panels. *Constr. Build. Mater.* **2017**, *139*, 45–51. [[CrossRef](#)]
39. Maxwell, J.C. *A Treatise on Electricity and Magnetism Dover Publications, Unabridged 3rd ed.*; Dover Publications, Inc.: New York, NY, USA, 1954; Volume 1.
40. Wellander, N. Homogenization of the Maxwell Equations: Case II. Nonlinear Conductivity. *Appl. Math.* **2002**, *47*, 255–283. [[CrossRef](#)]
41. Angell, T.S.; Kirsch, A. The conductive boundary condition for Maxwell's equations. *SIAM J. Appl. Math.* **1992**, *52*, 1597–1610. [[CrossRef](#)]
42. Nemilov, S.V. The review of possible interrelations between ionic conductivity, internal friction and the viscosity of glasses and glass forming melts within the framework of Maxwell equations. *J. Non-Crystalline Solids* **2011**, *357*, 1243–1263. [[CrossRef](#)]
43. Goncharenko, A.V. Generalizations of the Bruggeman equation and a concept of shape-distributed particle composites. *Phys. Rev. E* **2003**, *68*, 041108. [[CrossRef](#)]
44. Tjaden, B.; Cooper, S.J.; Brett, D.J.; Kramer, D.; Shearing, P.R. On the origin and application of the Bruggeman correlation for analysing transport phenomena in electrochemical systems. *Curr. Opin. Chem. Eng.* **2016**, *12*, 44–51. [[CrossRef](#)]
45. Liu, H.; Zhang, G.; Li, D.; Wang, C.; Bai, S.; Li, G.; Wang, G. Three-dimensional multi-phase simulation of cooling patterns for proton exchange membrane fuel cell based on a modified Bruggeman equation. *Appl. Therm. Eng.* **2020**, *174*, 115313. [[CrossRef](#)]
46. Myers, M.T. Pore Modeling: Extending the Hanai-Bruggeman Equation. In Proceedings of the SPWLA 30th Annual Logging Symposium, Denver, CO, USA, 11–14 June 1989.
47. Sanjaya, C.S. Pore Size Effect on Heat Transfer through Porous Medium. Ph.D. Thesis, National University of Singapore, Singapore, 2011.
48. Skibinski, J.; Cwieka, K.; Ibrahim, S.H.; Wejrzanowski, T. Influence of pore size variation on thermal conductivity of open-porous foams. *Materials* **2019**, *12*, 2017. [[CrossRef](#)] [[PubMed](#)]
49. Chen, J.; Wang, H.; Xie, P.; Najm, H. Analysis of thermal conductivity of porous concrete using laboratory measurements and microstructure models. *Constr. Build. Mater.* **2019**, *218*, 90–98. [[CrossRef](#)]
50. Lewis, T.B.; Nielsen, L.E. Dynamic mechanical properties of particulate-filled composites. *J. Appl. Polym. Sci.* **1970**, *14*, 1449–1471. [[CrossRef](#)]
51. Nielsen, L.E. The thermal and electrical conductivity of two-phase systems. *Ind. Eng. Chem. Fundamentals* **1974**, *13*, 17–20. [[CrossRef](#)]
52. Pal, R. On the Lewis-Nielsen model for thermal/electrical conductivity of composites. *Compos. Part A Appl. Sci. Manuf.* **2008**, *39*, 718–726. [[CrossRef](#)]
53. Kochetov, R.; Korobko, A.V.; Andritsch, T.; Morshuis, P.H.F.; Picken, S.J.; Smit, J.J. Three-phase lewis-nielsen model for the thermal conductivity of polymer nanocomposites. In Proceedings of the 2011 Annual Report Conference on Electrical Insulation and Dielectric Phenomena, Cancun, Mexico, 16–19 October 2011; pp. 338–341. [[CrossRef](#)]
54. Montes-De-Oca, L.M.; Medina-Esquivel, R.; Zambrano-Arjona, M.; Martínez-Torres, P. Thermal detection of second critical micelle concentration in SDS and CTAB aqueous solutions using a modified Lewis-Nielsen effective thermal model. *J. Mol. Liq.* **2022**, *363*, 119864. [[CrossRef](#)]
55. Pietrak, K.; Wiśniewski, T.S. A review of models for effective thermal conductivity of composite materials. *J. Power Technol.* **2015**, *95*, 14–24.
56. Wang, X.J.; Niu, X.H.; Qiu, X.W.; Istikomah, N.; Wang, L.B. Thermal conductivity of porous polymer materials considering pore special-shape and anisotropy. *Express Polym. Lett.* **2021**, *15*, 319–328. [[CrossRef](#)]
57. Javierre, E.; Vuik, C.; Vermolen, F.; van der Zwaag, S. A comparison of numerical models for one-dimensional Stefan problems. *J. Comput. Appl. Math.* **2006**, *192*, 445–459. [[CrossRef](#)]
58. Visintin, A. *Models of Phase Transitions*; Springer Science & Business Media: Berlin/Heidelberg, Germany, 1996; Volume 26.
59. Gupta, S.C. *The Classical Stefan Problem: Basic Concepts, Modelling and Analysis with Quasi-Analytical Solutions and Methods*; Elsevier: Amsterdam, The Netherlands, 2017; Volume 45.
60. Caggiano, A.; Mankel, C.; Koenders, E. Reviewing theoretical and numerical models for PCM-embedded cementitious composites. *Buildings* **2018**, *9*, 3. [[CrossRef](#)]
61. Mankel, C.; Caggiano, A.; König, A.; Schicchi, D.S.; Sam, M.N.; Koenders, E. Modelling the thermal energy storage of cementitious mortars made with PCM-recycled brick aggregates. *Materials* **2020**, *13*, 1064. [[CrossRef](#)] [[PubMed](#)]
62. Voller, V.R.; Swaminathan, C.R.; Thomas, B.G. Fixed grid techniques for phase change problems: A review. *Int. J. Numer. Methods Eng.* **1990**, *30*, 875–898. [[CrossRef](#)]

63. Šavija, B.; Zhang, H.; Schlangen, E. Influence of microencapsulated phase change material (PCM) addition on (micro) mechanical properties of cement paste. *Materials* **2017**, *10*, 863. [[CrossRef](#)]
64. Dobri, A.; Tsiantis, A.; Papathanasiou, T.; Wang, Y. Investigation of transient heat transfer in multi-scale PCM composites using a semi-analytical model. *Int. J. Heat Mass Transf.* **2021**, *175*, 121389. [[CrossRef](#)]
65. Šavija, B.; Schlangen, E. Use of phase change materials (PCMs) to mitigate early age thermal cracking in concrete: Theoretical considerations. *Constr. Build. Mater.* **2016**, *126*, 332–344. [[CrossRef](#)]
66. Fachinotti, V.; Peralta, I.; Toro, S.; Storti, B.; Caggiano, A. Automatic Generation of High-Fidelity Representative Volume Elements and Computational Homogenization for the Determination of Thermal Conductivity in Foamed Concretes. 2022. Available online: <https://ssrn.com/abstract=4286262> (accessed on 15 August 2023).
67. Batool, F. Effect of Microstructure on Thermal Conductivity of Cement-Based Foam. Ph.D. Thesis, University of Alberta Libraries, Edmonton, AB, Canada, 2015.
68. Awang, H.; Mydin, M.A.O.; Roslan, A.F. Effect of additives on mechanical and thermal properties of lightweight foamed concrete. *Adv. Appl. Sci. Res.* **2012**, *3*, 3326–3338.
69. Wei, S.; Yiqiang, C.; Yunsheng, Z.; Jones, M. Characterization and simulation of microstructure and thermal properties of foamed concrete. *Constr. Build. Mater.* **2013**, *47*, 1278–1291. [[CrossRef](#)]
70. Mydin, M.A.O. Effective thermal conductivity of foamcrete of different densities. *Concr. Res. Lett.* **2011**, *2*, 181–189.
71. Davraz, M.; Kilinçarslan, Ş.; Koru, M.; Tuzlak, F. Investigation of relationships between ultrasonic pulse velocity and thermal conductivity coefficient in foam concretes. *Acta Phys. Pol. A* **2016**, *130*, 469–470. [[CrossRef](#)]
72. Oren, O.H.; Gholampour, A.; Gencel, O.; Ozbakkaloglu, T. Physical and mechanical properties of foam concretes containing granulated blast furnace slag as fine aggregate. *Constr. Build. Mater.* **2019**, *238*, 117774. [[CrossRef](#)]
73. Jiang, J.; Lu, Z.; Niu, Y.; Li, J. Investigation of the properties of high-porosity cement foams containing epoxy resin. *Constr. Build. Mater.* **2017**, *154*, 115–122. [[CrossRef](#)]
74. Jiang, J.; Lu, Z.; Niu, Y.; Li, J.; Zhang, Y. Investigation of the properties of high-porosity cement foams based on ternary Portland cement–metakaolin–silica fume blends. *Constr. Build. Mater.* **2016**, *107*, 181–190. [[CrossRef](#)]
75. Neville, A.M.; Brooks, J.J. *Concrete Technology*; Longman Scientific & Technical: New York, NY, USA, 1987; Volume 438.
76. Tran, N.P.; Nguyen, T.N.; Ngo, T.D.; Le, P.K.; Le, T.A. Strategic progress in foam Stabilization towards high-performance foam concrete for building sustainability: A state-of-the-art review. *J. Clean. Prod.* **2022**, *375*, 133939. [[CrossRef](#)]
77. Kern, T. Neues Verfahren zur experimentellen Untersuchung wässriger Schäume. Ph.D Thesis, University of Paderborn, Paderborn, Germany, 2002.
78. Lohaus, L.; Pott, J.U. *Konstruktionsleichtbeton unter Verwendung Vorgeschaumter Luftporen*; Forschungsbericht; Institut für Baustoffe, Universität Hannover: Hanover, Germany, 2005; Available online: <https://www.baustoff.uni-hannover.de/de/forschung/forschungsprojekte/forschungsprojekte-detailansicht/projects/konstruktionsleichtbeton-unter-verwendung-vorgeschaemter-luftporen/> (accessed on 15 August 2023).
79. Pott, J.U. Entwicklungsstrategien für zementgebundene Schäume. IfB. 2006. Available online: <https://www.baustoff.uni-hannover.de/fileadmin/baustoff/publications/Heft05-Pott-ZemSchaum.pdf> (accessed on 15 August 2023).
80. Sam, M.; Caggiano, A.; Dubyey, L.; Dauvergne, J.-L.; Koenders, E. Thermo-physical and mechanical investigation of cementitious composites enhanced with microencapsulated phase change materials for thermal energy storage. *Constr. Build. Mater.* **2022**, *340*, 127585. [[CrossRef](#)]
81. Available online: https://issuu.com/detail-magazine/docs/978-3-920034-18-8_bk_de_daemmstoffe (accessed on 15 August 2023).
82. Schild, K. *Wärmeschutz: Grundlagen-Berechnung-Bewertung*; Springer: Berlin/Heidelberg, Germany, 2013.

Disclaimer/Publisher’s Note: The statements, opinions and data contained in all publications are solely those of the individual author(s) and contributor(s) and not of MDPI and/or the editor(s). MDPI and/or the editor(s) disclaim responsibility for any injury to people or property resulting from any ideas, methods, instructions or products referred to in the content.